



# Space Telescope and Optical Reverberation Mapping Project. X. Understanding the Absorption-line Holiday in NGC 5548

M. Dehghanian<sup>1</sup> , G. J. Ferland<sup>1</sup> , G. A. Kriss<sup>2</sup> , B. M. Peterson<sup>2,3,4</sup> , S. Mathur<sup>3,4</sup>, M. Mehdipour<sup>5</sup>, F. Guzmán<sup>1</sup> , M. Chatzikos<sup>1</sup>, P. A. M. van Hoof<sup>6</sup> , R. J. R. Williams<sup>7</sup> , N. Arav<sup>8</sup>, A. J. Barth<sup>9</sup> , M. C. Bentz<sup>10</sup> , S. Bisogni<sup>3,11,12</sup> , W. N. Brandt<sup>13,14,15</sup> , D. M. Crenshaw<sup>10</sup> , E. Dalla Bontà<sup>16,17</sup>, G. De Rosa<sup>2</sup> , M. M. Fausnaugh<sup>3,18</sup> , J. M. Gelbord<sup>19,20</sup>, M. R. Goad<sup>21</sup>, A. Gupta<sup>3</sup> , Keith Horne<sup>22</sup> , J. Kaastra<sup>5,23</sup> , C. Knigge<sup>24</sup>, K. T. Korista<sup>25</sup> , I. M. McHardy<sup>24</sup>, R. W. Pogge<sup>3,4</sup> , D. A. Starkey<sup>22,26</sup>, and M. Vestergaard<sup>27,28</sup>

<sup>1</sup> Department of Physics and Astronomy, The University of Kentucky, Lexington, KY 40506, USA

<sup>2</sup> Space Telescope Science Institute, 3700 San Martin Drive, Baltimore, MD 21218, USA

<sup>3</sup> Department of Astronomy, The Ohio State University, 140 W 18th Avenue, Columbus, OH 43210, USA

<sup>4</sup> Center for Cosmology and AstroParticle Physics, The Ohio State University, 191 West Woodruff Avenue, Columbus, OH 43210, USA

<sup>5</sup> SRON Netherlands Institute for Space Research, Sorbonnelaan 2, 3584, CA Utrecht, The Netherlands

<sup>6</sup> Royal Observatory of Belgium, Ringlaan 3, B-1180 Brussels, Belgium

<sup>7</sup> AWE plc, Aldermaston, Reading RG7 4PR, UK

<sup>8</sup> Department of Physics, Virginia Tech, Blacksburg, VA 24061, USA

<sup>9</sup> Department of Physics and Astronomy, 4129 Frederick Reines Hall, University of California, Irvine, CA 92697, USA

<sup>10</sup> Department of Physics and Astronomy, Georgia State University, 25 Park Place, Suite 605, Atlanta, GA 30303, USA

<sup>11</sup> Osservatorio Astrofisico di Arcetri, largo E. Fermi 5, I-50125, Firenze, Italy

<sup>12</sup> Harvard-Smithsonian Center for Astrophysics, 60 Garden Street, Cambridge, MA 02138, USA

<sup>13</sup> Department of Astronomy and Astrophysics, Eberly College of Science, The Pennsylvania State University, 525 Davey Laboratory, University Park, PA 16802, USA

<sup>14</sup> Department of Physics, The Pennsylvania State University, 104 Davey Laboratory, University Park, PA 16802, USA

<sup>15</sup> Institute for Gravitation and the Cosmos, The Pennsylvania State University, University Park, PA 16802, USA

<sup>16</sup> Dipartimento di Fisica e Astronomia “G. Galilei,” Università di Padova, Vicolo dell’Osservatorio 3, I-35122 Padova, Italy

<sup>17</sup> INAF-Osservatorio Astronomico di Padova, Vicolo dell’Osservatorio 5 I-35122, Padova, Italy

<sup>18</sup> Kavli Institute for Space and Astrophysics Research, Massachusetts Institute of Technology, 77 Massachusetts Avenue, Cambridge, MA 02139-4307, USA

<sup>19</sup> Spectral Sciences Inc., 4 Fourth Avenue, Burlington, MA 01803, USA

<sup>20</sup> Eureka Scientific Inc., 2452 Delmer Street, Suite 100, Oakland, CA 94602, USA

<sup>21</sup> Department of Physics and Astronomy, University of Leicester, University Road, Leicester, LE1 7RH, UK

<sup>22</sup> SUPA Physics and Astronomy, University of St. Andrews, Fife, KY16 9SS Scotland, UK

<sup>23</sup> Leiden Observatory, Leiden University, P.O. Box 9513, 2300 RA Leiden, The Netherlands

<sup>24</sup> School of Physics and Astronomy, University of Southampton, Highfield, Southampton, SO17 1BJ, UK

<sup>25</sup> Department of Physics, Western Michigan University, 1120 Everett Tower, Kalamazoo, MI 49008-5252, USA

<sup>26</sup> Department of Astronomy, University of Illinois Urbana-Champaign, 1002 W. Green Street, Urbana, IL 61801, USA

<sup>27</sup> DARK, Niels Bohr Institute, University of Copenhagen, Vibenshuset, Lyngbyvej 2, DK-2100 Copenhagen Ø, Denmark

<sup>28</sup> Steward Observatory, University of Arizona, 933 North Cherry Avenue, Tucson, AZ 85721, USA

Received 2018 December 29; revised 2019 April 18; accepted 2019 April 20; published 2019 June 3

## Abstract

The Space Telescope and Optical Reverberation Mapping Project (AGN STORM) on NGC 5548 in 2014 is one of the most intensive multiwavelength AGN monitoring campaigns ever. For most of the campaign, the emission-line variations followed changes in the continuum with a time lag, as expected. However, the lines varied independently of the observed UV-optical continuum during a 60–70 day “holiday,” suggesting that unobserved changes to the ionizing continuum were present. To understand this remarkable phenomenon and to obtain an independent assessment of the ionizing continuum variations, we study the intrinsic absorption lines present in NGC 5548. We identify a novel cycle that reproduces the absorption line variability and thus identify the physics that allows the holiday to occur. In this cycle, variations in this obscurer’s line-of-sight covering factor modify the soft X-ray continuum, changing the ionization of helium. Ionizing radiation produced by recombining helium then affects the level of ionization of some ions seen by the *Hubble Space Telescope*. In particular, high-ionization species are affected by changes in the obscurer covering factor, which does not affect the optical or UV continuum, and thus appear as uncorrelated changes, a “holiday.” It is likely that any other model that selectively changes the soft X-ray part of the continuum during the holiday can also explain the anomalous emission-line behavior observed.

**Key words:** galaxies: active – galaxies: individual (NGC 5548) – galaxies: nuclei – galaxies: Seyfert – line: formation

## 1. Introduction

In 2013, NGC 5548 was the subject of an intensive monitoring campaign based primarily on X-ray data from *XMM-Newton* and the *Neil Gehrels Swift Observatory*, supplemented with spectra from the *Hubble Space Telescope* (*HST*) Cosmic Origins Spectrograph (Kaastra et al. 2014;



Original content from this work may be used under the terms of the [Creative Commons Attribution 3.0 licence](https://creativecommons.org/licenses/by/3.0/). Any further distribution of this work must maintain attribution to the author(s) and the title of the work, journal citation and DOI.

Arav et al. 2015; Di Gesu et al. 2015; Mehdipour et al. 2015, 2016; Ursini et al. 2015; Whewell et al. 2015; Cappi et al. 2016; Ebrero et al. 2016). In the following year, an intensive ultraviolet and optical reverberation mapping program (the Space Telescope and Optical Reverberation Mapping program, or AGN STORM) was undertaken using *HST* (De Rosa et al. 2015; G. A. Kriss et al. 2019, in preparation), the *Neil Gehrels Swift Observatory* (Edelson et al. 2015), ground-based telescopes for both imaging (Fausnaugh et al. 2016) and spectroscopy (Pei et al. 2017), and the *Chandra X-Ray Observatory* (Mathur et al. 2017). This program yielded the first high-fidelity measurements of interband continuum lags in NGC 5548 (Edelson et al. 2015; Fausnaugh et al. 2016; Starkey et al. 2017) and some very surprising emission-line results (Goad et al. 2016; Pei et al. 2017)—in particular, some 60 days into the campaign, the broad emission lines stopped responding strongly to continuum variations. However, by the end of the six-month campaign, the normal relationship between the continuum and broad emission lines was restored. To the AGN STORM team, it appeared as though the BLR had “gone on a holiday” and for that reason we will continue to refer to the period of anomalous emission-line response as the “BLR holiday.”

It was subsequently noted (G. A. Kriss et al. 2019, in preparation) that the behavior of the narrow absorption lines changed during the BLR holiday, with the lower-ionization lines continuing to track the observed UV continuum, but with only decorrelated changes in the higher-ionization absorption lines. These holidays are not a prediction of photoionization theory and the current standard model of the geometry of an AGN. Understanding the physics behind the holiday is essential because line-continuum reverberation is the only direct way to measure the mass of the central black hole, and this method is based on the existence of a correlation between the continuum and broad emission lines. The purpose of this paper is to begin an exploration of the BLR holiday phenomenon by examining the behavior of the narrow absorption lines, drawing extensively from the results obtained during the 2013 *XMM-Newton* program as well as the 2014 AGN STORM campaign. We focus on the absorption lines because the geometry is much simpler than the emission-line geometry. Absorbing gas must lie along our line of sight and the clouds must see the same spectral energy distribution (SED) as we do. Later sections discuss the observational constraints on the physics behind the holiday. We identify a novel physical process in which changes in the SED cause changes in the ionization of helium, which then drives the absorption line changes observed by *HST*.

## 2. The Geometry and the Obscurer

Historically, our line of sight to the central regions of NGC 5548 has been fairly clear, with no heavy obscuration in the soft X-ray, although “warm absorbers” are present (Mathur et al. 1995; Kaastra et al. 2000). Dramatic changes in the broadband soft X-ray absorption occurred and were interpreted as being due to a cloud, “the obscurer,” passing across our line of sight (Kaastra et al. 2014; Mehdipour et al. 2016). This kind of heavy obscuration had never been seen before in NGC 5548 although a similar extinction occurred in NGC 4151 (Ferland & Mushotzky 1982). Soft X-ray absorption by the obscurer was first observed in NGC 5548 in 2012 and 2013 (Arav et al. 2015; Mehdipour et al. 2016). Here we briefly summarize the

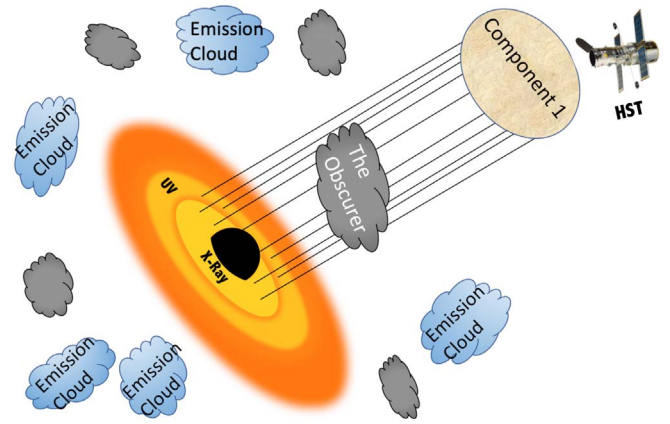


**Figure 1.** Geometry of the emission and absorption components discussed in this paper. The line-of-sight obscurer covers 70%–100% of the X-ray source (Mehdipour et al. 2016). The gray clouds show other possible obscurers. These will be discussed in the next paper in this series. The blue blobs indicate the BLR clouds surrounding the source. Component 1, the narrow absorption line component with the highest outflow velocity ( $-1165 \text{ km s}^{-1}$ ), is also shown. Component 1 is the absorbing component studied in this paper.

geometry inferred by the *XMM-Newton* “Anatomy” series of papers (Kaastra et al. 2014; Arav et al. 2015; Mehdipour et al. 2015, 2016; Ursini et al. 2015). Figure 1 shows a sketch of the overall geometry, including the black hole and accretion disk, which produce the intrinsic (unobscured) SED. The observer is located in the direction of the *HST* icon.

A set of six intrinsic, narrow FUV<sup>29</sup> absorption lines potentially associated with the X-ray warm absorber in NGC 5548 (Mathur et al. 1995) have been studied in detail by Mathur et al. (1999), Crenshaw et al. (2003), Arav et al. (2015), and G. A. Kriss et al. (2019, in preparation). They are numbered from 1 to 6 in order of decreasing outflow velocity from  $-1165$  to  $+250 \text{ km s}^{-1}$ . In this paper, we specifically study the cloud producing Component 1, which is also illustrated in Figure 1. Component 1 is the closest narrow FUV absorber to the central source, and it is the target of our study because it shows the most dramatic changes during the obscuration (Arav et al. 2015). This component also has the greatest assortment of associated UV absorption lines, permitting its characteristics to be determined in detail. The full physical properties of this component were derived by Arav et al. (2015). In particular, it has a density of  $\log n_e = 4.8 \pm 0.1 \text{ cm}^{-3}$ , as measured using the metastable absorption lines of C III and Si III. This leads to a well determined distance of  $3.5 \pm 0.1 \text{ pc}$ , placing it outside the BLR but within the narrow line region (Peterson et al. 1999).

Little is known about the density and location of the obscurer, but the ionization state, inferred high density, the kinematics, absorption line profiles, and the covering factors all suggest an origin in the BLR (Kaastra et al. 2014; Di Gesu et al. 2015; Mehdipour et al. 2015). BLR lags of 2 days to  $\sim 10$  days would imply a distance of between  $6 \times 10^{15}$  and  $3 \times 10^{16} \text{ cm}$  (De Rosa et al. 2015). The soft X-ray observations show that the obscurer does not fully cover the X-ray source. The covering factor varied between 0.7 and 1.0 over the period 2012–2015 (Mehdipour et al. 2016). This change may be caused by either transverse motions of the obscurer, changes in

<sup>29</sup> We refer to region 6–13.6 eV (912–2000 Å) as FUV; 13.6–54.4 eV (228–912 Å) as EUV; and 54.4 eV to few hundred eV (less than 228 Å) as XUV.

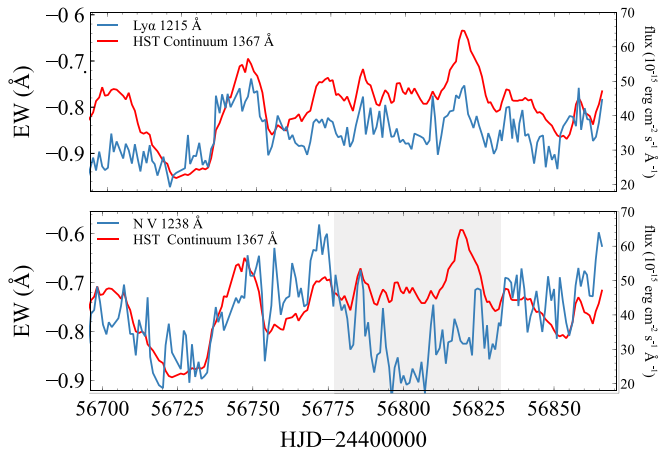


**Figure 2.** Both panels show the arbitrarily scaled FUV continuum in red, as a function of Heliocentric Julian Date  $-24,400,000$ . The upper panel shows the equivalent width of the  $\text{Ly}\alpha$  absorber of Component 1 in blue and the lower panel shows the equivalent width of the corresponding  $\text{N V } \lambda 1238$  absorption line. Shaded area indicates the time in which the “holiday” is happening.

its internal structure, or changes in the size of the X-ray source (Mehdipour et al. 2016). Finally, it is possible that other obscurers lie within the central regions, as shown in Figure 1.

### 3. The Holiday

In photoionization equilibrium, there is a correlation between the brightness of the ionizing radiation field and the ionization state of the gas. Reverberation measurements rely on this, with the only complication being the time lag caused by the finite speed of light. “Holidays,” where the correlation breaks down, are not expected. This section outlines the absorption and emission-line holidays that occurred during the AGN STORM campaign.

#### 3.1. Broad Emission Lines and Their Holiday

The AGN STORM campaign monitored NGC 5548 for the 6 month period from 2014 January to July. During almost 120 days of the campaign, the BLR emission exhibited the expected correlation with the continuum. The line and continuum emission holiday started about 75 days after the first *HST* observation and continued for 60–70 days (Goad et al. 2016). The lines then returned to their normal behavior. Goad et al. (2016) and Pei et al. (2017) note that the strong and broad emission lines became significantly fainter (e.g., in C IV and  $\text{H}\beta$ ) during the holiday. This is the best-characterized anomalous event detected in a reverberation mapping campaign.

#### 3.2. Narrow Absorption Lines and Their Holiday

Some, but not all, of the Component 1 absorption lines displayed a holiday similar to the emission lines. Three low-ionization species—H I, Si II, and C II—showed good correlations with the *HST* FUV continuum, while the higher-ionization species—Si III, Si IV, C III, C IV, and N V—showed decorrelated behavior (G. A. Kriss et al. 2019, in preparation). Figure 2 shows examples of both behaviors,  $\text{Ly}\alpha$  and  $\text{N V } \lambda 1238$ . The red line shows the arbitrarily scaled *HST* FUV continuum while the blue lines are Component 1 absorption line equivalent widths (EWs). Both lines correlate

for most of the campaign, but, like the broad emission lines, there is an almost 70 day period when N V is decorrelated.

#### 3.3. The Scope of This Paper

This paper focuses on the absorption line holiday with the aim of reproducing the correlation/decorrelation shown in Figure 2. As Figure 1 shows, the absorption lines involve an especially simple geometry with the continuum emitters and absorbers lying along a single line of sight and the absorbing clouds being illuminated by the SED directed toward the Earth. The absorption lines vary due to changes in the SED striking Component 1. These changes may be due to variations of the brightness of the AGN or changes in the shape of the SED caused by changes in the obscurer’s absorption.

The emission lines are more complicated. They might not be directly affected by the obscurer because they lie along different sight lines from the AGN (Figure 1). Other obscurers may be present on other sight lines and could affect the emission lines. The emitting clouds have a range of densities and distances from the center. All of this introduces complexities. The absorption lines are the simplest, and so the best place to start studying the physics behind the holiday. They are the focus of this paper.

The remainder of the paper examines how an absorption line holiday can occur. Our goal is to identify a physical process whereby lines sometime correlate with the observed FUV continuum, and at other times do not. We aim to identify the phenomenology that makes this possible, but not model any particular *HST* observation. Converting between observed EWs and the ionic column densities we predict requires a curve of growth analysis. This brings in additional uncertainties including the velocity field of the gas and possible substructure within the absorption lines. The presence or absence of a correlation between the FUV continuum and a line EW or column density will not be affected by curve of growth effects. In other words, we want to reproduce the correlation/decorrelation of the lines and continuum and do not model specific derived column densities. We build upon the Arav et al. (2015) model of Component 1 and do not change its basic assumptions. In the following section we present the standard parameters for Component 1, taken from Arav et al. (2015).

### 4. The “Standard” Model of Component 1

Below we use photoionization models to investigate why some absorption lines correlate with the FUV continuum and some do not. We first adopt the intrinsic SED emitted by the accretion disk, shown in Figure 3. This was derived by continuum modeling during the multiwavelength campaign data on NGC 5548 (Mehdipour et al. 2015) and is used in all calculations presented below. This is based on a Comptonized thermal accretion disk model. This model was derived using simultaneous, coordinated multiwavelength observations including FUV and soft X-ray (Kaastra et al. 2014) and hard X-ray continua (Ursini et al. 2015). This SED was incorporated into the developmental version of *cloudy*, most recently described by Ferland et al. (2017), and will be available in the next release. We use this developmental version throughout this paper. Version 17, the latest public release of *cloudy*, included an NGC 5548 SED derived by Tek P. Adhikari from CAMK (Warsaw), by digitizing Figure 10 of Mehdipour et al. (2015). That SED did not include data for energies not included

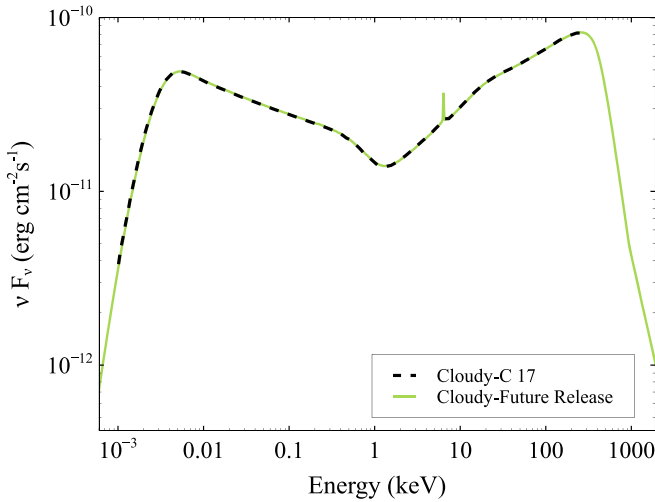


**Figure 3.** Intrinsic (unobscured) SED available in version 17 of *cloudy* (C17) is shown by the dashed black line. It was zero outside the indicated range. The green line shows the improved SED (Mehdipour et al. 2015), which will be implemented in future versions of *cloudy*.

in the published figure. The improved SED used by Mehdipour et al. (2015) covers the entire electromagnetic spectrum, and includes the observed Fe K $\alpha$  line.

The principal conclusion of Hopkins et al. (2004) is that extinction in SDSS quasars is typically  $E(B - V) = 0.013$  mag with an SMC-like extinction curve. There are, of course, red quasars that are heavily extinguished (Gaskell 2017), but NGC 5548 is not one of them. There are hard X-ray observations with *NuSTAR* and *INTEGRAL* observatories, and the SED model that we use matches the observed flux and shape of the hard X-ray continuum (Ursini et al. 2015). The SED model that was derived by Mehdipour et al. (2015) is fully consistent with simultaneous observations taken with multiple observatories from optical to hard X-rays.

We adopt the obscurer parameters— $N(\text{H}) = 1.2 \times 10^{22} \text{ cm}^{-2}$  and  $\log \xi = -1.2$  ( $\text{erg cm s}^{-1}$ )—derived by Kaastra et al. (2014). The ionization parameter  $\xi$  is defined as (Tarter et al. 1969; Kallman & Bautista 2001)

$$\xi = \frac{L}{n(\text{H})R^2}, \quad (1)$$

where  $L$  is the luminosity of the ionizing source over the 1–1000 Ryd (13.6 eV–13.6 keV) band in  $\text{erg s}^{-1}$ ,  $R$  is the distance from the source in centimeters. For the hydrogen density, we adopt  $n(\text{H}) = 10^{10} \text{ cm}^{-3}$ , which is a typical BLR cloud density. We adopt the *cloudy* default value<sup>30</sup> for solar abundances, which are generally within 30% of the Lodders (2003) meteoritic abundances used in some of the previous modeling. The transmitted SED calculated with these parameters is shown in Figure 4, in which we assume that the obscurer fully covers the continuum source. This figure shows the net transmitted radiation field at the shielded face of the obscurer. It includes the attenuated incident radiation field produced by the central object along with line and continuum emission produced by the obscurer. The effects of filtering the continuum have been discussed in other literature but within

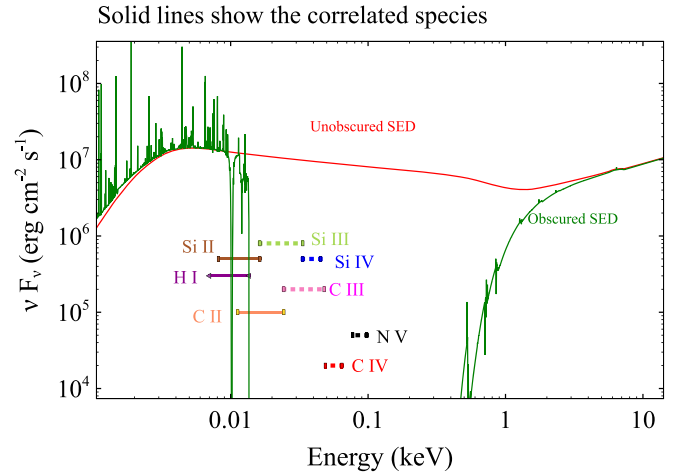


**Figure 4.** The SED transmitted through the obscurer and striking Component 1. Each line segment shows the energy required to produce the ion (left end) and to destroy the ion (right end). In this figure, we assumed that the obscurer fully covers the continuum source. The column density to make the transmitted SED is  $N(\text{H}) = 1.2 \times 10^{22} \text{ cm}^{-2}$ .

different contexts (Ferland & Mushotzky 1982; Leighly 2004). The horizontal lines in Figure 4 indicate the ionization energies for the species studied by G. A. Kriss et al. (2019, in preparation). The left terminus of each line shows the energy needed to produce the ion, while the right terminus indicates the amount of energy required to destroy the ion by further ionization. The high-ionization-potential species (indicated by dotted lines) did not correlate with the FUV during the holiday, while lower-ionization-potential species (solid lines) remained correlated.

In the case of Component 1, we adopt the parameters from Arav et al. (2015),  $\log n(\text{H}) = 4.72$  ( $\text{cm}^{-3}$ ) and ionization parameter  $\log U = -1.5$ , which is defined to be (Osterbrock & Ferland 2006):

$$U = \frac{Q(\text{H})}{4\pi R^2 n(\text{H})c}, \quad (2)$$

where  $Q(\text{H})$  is the number of hydrogen-ionizing photons emitted by the source per second,  $R$  is the cloud distance from the ionizing continuum source, which is 3–5 pc for Component 1 as described in Section 2. In the above equation,  $c$  is the speed of light. Note that the papers modeling the obscurer (Kaastra et al. 2014) and Component 1 (Arav et al. 2015) use different definitions for the ionization parameter. For the unobscured SED, the relation  $\log U = \log \xi - 1.6$  can be used to convert between these ionization parameters. For the obscured SED (Figure 4, green line), the conversion relation is  $\log U = \log \xi - 3.3$ .

## 5. What Happened?

We hypothesize that two independent events occurred. First, the luminosity of the AGN varied, causing the entire SED to become brighter or fainter. This would cause the expected correlated variations. Second, the obscurer moved across our line of sight, perhaps due to its orbital motion around the black hole, changing the fraction of the central source that is covered. We will show below that absorption by the obscurer changes

<sup>30</sup> More information about the default values can be found in HAZY: <https://www.nublado.org/wiki/DownloadLinks>.

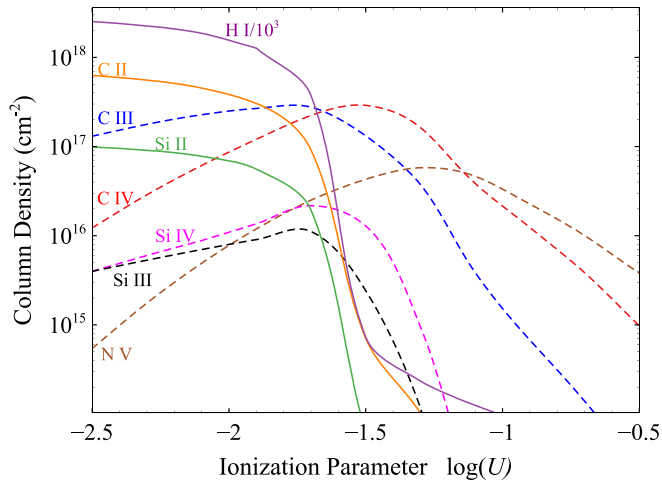


**Figure 5.** This figure shows how Component 1 column densities change as the ionization parameter changes. The hydrogen column density is divided by 1000 for comparison purposes. The solid lines are correlated species while the dashed lines are decorrelated. These changes are unlike those seen in the holiday, ruling out changes in  $U$  alone as the reason for the holiday.

the EUV, XUV, and soft X-ray portions of the SED but has little effect on the optical, UV, or FUV, where the obscurer is transparent. This variable absorption, caused by the changing covering factor, would affect the high-ionization absorption lines but have little effect on the FUV or optical continuum, so would produce decorrelated changes i.e., a “holiday.” In the rest of this section, we investigate these two events in more detail.

### 5.1. Changing the Luminosity of the Source

The changing luminosity is directly seen via optical, FUV, and X-ray observations. In photoionization equilibrium, this implies a varying ionization parameter, which would change the column densities of all species. As a test, we checked what happens to the column densities of Component 1 absorbing species when the continuum luminosity changes, while keeping the unobscured shape of the SED the same. We use the Arav et al. (2015) standard Component 1 parameters as described above, but we let the ionization parameter  $U$  vary by one dex to either side of the standard value of  $\log U = -1.5$ . This would correspond to changes in the continuum luminosity by the same amount. For comparison, the 1157 Å *HST* continuum varied over a range of 0.6 dex during the STORM campaign. Figure 5 shows the results of these calculations. The solid lines show the correlated species while the dashed lines are decorrelated. All the column densities change dramatically; however, around the standard value of  $\log U = -1.5$ , the columns of the correlated species are changing very fast, faster than those of the decorrelated ones. This is not enough to explain the holiday. Thus, simple changes in the luminosity of NGC 5548 cannot explain the absorption line holiday. We must look elsewhere.

### 5.2. Changing the Obscurer Covering Factor

The soft X-ray extinction measures the fraction of the continuum source covered by the obscurer. We refer to this as the “line-of-sight covering factor” (LOS CF). Changes in the LOS CF affect the absorption lines seen with *HST* because the SED transmitted through the obscurer is responsible for the ionization of Component 1. Figure 6 shows how changes in

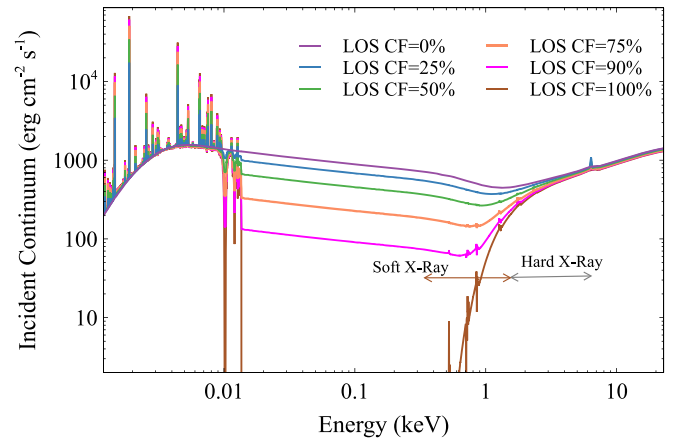


**Figure 6.** Variations of the SED striking Component 1 for different LOS CFs. The Arav et al. (2015) ionization parameter is reproduced at zero coverage. The figure indicates the soft and hard X-ray energies, i.e., 0.3–1.5 and 1.5–10 keV (Mehdipour et al. 2016).

the LOS CF affect  $\text{SED}_{\text{inc}}$ , the SED striking Component 1. This is defined as:

$$\text{SED}_{\text{inc}} = (\text{LOS CF}) \times (\text{SED}_{\text{extinguished}}) + (1 - \text{LOS CF}) \times \text{SED} \quad (3)$$

for various LOS CF. Here “SED” indicates the unattenuated SED shown in Figure 3. The intensity is adjusted to  $\log U = -1.5$  with LOS CF = 0 (Arav et al. 2015). We keep the brightness of  $\text{SED}_{\text{inc}}$  constant at 4558 Å (0.2 Ryd), and vary the LOS CF to obtain different shapes. We chose the energy 0.2 Ryd because this is an energy where the obscurer is transparent. In Equation (3), LOS CF = 0 will be the full unattenuated SED and 100% coverage would be the Mehdipour et al. (2015) extinguished SED (Figure 4). Figure 6 shows that the 1 keV X-ray absorption is highly affected by changes in the LOS CF. The hard X-rays are not absorbed and so do not change. Note that this assumes that the LOS CF is the same for the EUV and XUV, whereas these components may form in different regions (Gardner & Done 2017; Edelson et al. 2019). Note that the SEDs shown in Figure 6 are the *incident* radiation field striking the illuminated face of Component 1. The data come from the second column of the `cloudy save continuum`. The effects of diffuse fields from the obscurer are included when generating the extinguished SED.

Variations of the obscurer LOS CF produce considerable changes in the transmitted SED without producing observable changes in the FUV because the obscurer is transparent in the FUV (see Figure 6). Perhaps this can provide an explanation for the correlated and decorrelated behavior of the narrow absorption lines of Component 1. Next, we investigate how the column densities of Component 1 are affected by the changes in the obscurer LOS CF. We used SEDs like those illustrated in Figure 6 to predict the column densities of the Component 1 species measured by G. A. Kriss et al. (2019, in preparation). These are shown in Figure 7. The column densities of high-ionization species decrease while low-ionization species change little at high LOS CF values. Clearly, then, changes in the obscurer LOS CF are capable of causing the absorption line holiday. The next section outlines the physics behind Figure 7.

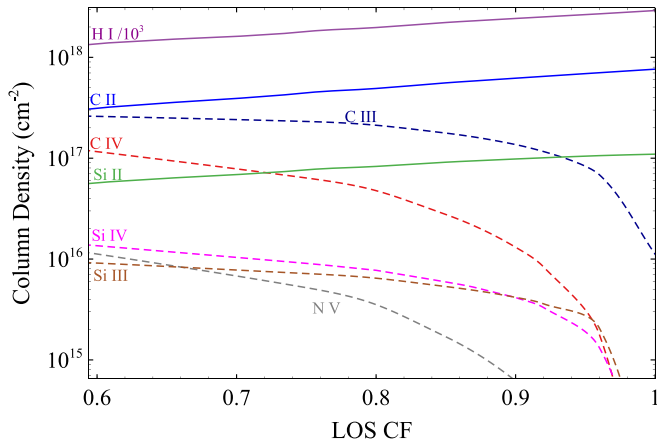


**Figure 7.** Effects of changes in the obscurer LOS CF upon the column densities observed by *HST*. Low-ionization species (solid lines) remained correlated while high-ionization (dashed) species were decorrelated during the holiday, as expected from changes in the obscurer covering factor. The ionization parameters adopted for the obscurer and Component 1 are  $\log \xi = -1.2$  ( $\text{erg cm s}^{-1}$ ) and  $\log U = -1.5$ , respectively.

## 6. Physics Behind the “Holiday”

Figure 7 focused on the absorption line species observed in the *HST* spectra. These are not necessarily the dominant or most important ions. Figure 8 shows how the physically important ions change, and includes helium, which *HST* did not observe. Silicon and carbon are mainly singly ionized, while He is mostly neutral.

As the LOS CF increases, the column densities of the higher-ionization-potential decorrelated ions decrease dramatically, as also seen in Figure 7. The ions  $\text{He}^+$  and  $\text{He}^{+2}$  behave like the higher-ionization-potential decorrelated species.  $\text{Si}^+$  and  $\text{C}^+$  are the most abundant ions, and their column densities change only slightly. To understand this behavior, we must isolate what photoionizes the dominant and correlated low-ionization species to produce the decorrelated behavior in the higher-ionization species. To answer this, we consider the radiation field within Component 1. Figure 9 shows the diffuse radiation field at the midplane, the middle of the Component 1 cloud. The midplane is a representative location, and its properties give insight into the physics of the cloud. We chose an LOS CF of 96%, which is representative of the regions of Figure 7 where the correlated/decorrelated behavior is pronounced. This covering factor is so large that the EUV and XUV portion of the incident SED shown in Figure 6 is faint. The diffuse radiation field shown is produced by emission from the absorbing gas itself and is dominated by line and continuum emission produced by recombining helium. Several of the prominent emission features are labeled. The horizontal lines indicate the range of photon energy that can photoionize the indicated species.

Examination of the photoionization rates shows that  $\text{C}^+$  and  $\text{Si}^+$  are produced by photoionization of the neutral atoms by the Balmer continuum. They are destroyed by valence-shell photoionization, with thresholds of 24.4 eV and 16.3 eV for  $\text{C}^+$  and  $\text{Si}^+$ , respectively. Inner shell photoionization by the soft X-rays is much less important. The He I radiative recombination continua (for  $\text{C}^+$  and  $\text{Si}^+$ ) and singlet and triplet  $2p - 1s$  transitions of  $\text{He}^0$  (for  $\text{Si}^+$ ) are the primary sources of photoionization at energies of  $\sim 20$ – $25$  eV, the threshold for destroying these dominant species. These are all produced by

recombination of  $\text{He}^+$ . This means that the abundances of the decorrelated high-ionization species follow the abundance of  $\text{He}^+$  and subsequent He I emission. Figure 8 shows that the decrease in column density of the decorrelated species tracks changes in the  $\text{He}^+$  column density. What is responsible for photoionization of  $\text{He}^0$ , producing  $\text{He}^+$ ?  $\text{He}^0$  is the dominant ion stage in Component 1 (Figure 8). Examination of the contributors to the photoionization rates shows that  $\text{He}^+$  is produced through photoionization by soft X-rays from the attenuated SED of the AGN. Figure 9 shows only the diffuse fields and does not include the attenuated incident SED.  $\text{He}^0$  is an important opacity source for soft X-rays. Figure 10 shows the continuous opacity at the midplane of the Component 1 cloud. We evaluated the total gas opacity for the predicted distribution of ions and the assumed solar composition. This shows the opacity per hydrogen and is multiplied by the cube of the photon energy so that it can be compared with standard plots of the total ISM opacity (Ride & Walker 1977). The green line shows the total opacity while the other lines show some of the important contributors to it.  $\text{H}^0$  is dominant in the low-energy EUV,  $\text{He}^0$  is dominant in the high-energy EUV and XUV, and the heavy elements dominate around 0.5–1 keV (Crudace et al. 1974; Ride & Walker 1977, their Figure 2), causing the stepped rise in the right part of the diagram. Helium is mainly neutral (Figure 8) and Figure 10 shows that helium is a major contributor to the total opacity for energies from 24 to 300 eV.

The gas photoionization rate is the integral of the opacity shown in Figure 10 over the radiation field shown in Figure 9 (see Osterbrock & Ferland 2006, Equation (2.30)). It is critical to know which part of the radiation field dominates the total photoionization rate, because this has the greatest effect on the ionization of Component 1. This is shown in the lower panel of Figure 11. This panel shows the values of the terms entering in the photoionization rate integral, namely the product  $\nu^2(4\pi J_\nu/h\nu) \times \alpha_\nu$ . In this equation,  $\alpha_\nu$  is the opacity and  $J_\nu$  is the mean intensity. This shows the coupling between the radiation and the gas. Only interactions at energies greater than 13.6 eV affect the ionization of the gas, and the strongest coupling occurs at energies between  $\sim 200$  eV and  $\sim 2$  keV. When the LOS CF varies, the soft X-rays change, as shown in Figure 6. This carries over into changes in the ionization of  $\text{He}^0$ . This leads to changes in the  $\text{He}^0$  EUV recombination radiation, which produces the highly ionized species seen by *HST*.

The upper panel of Figure 11 shows the incident SED as a solid blue line. The solid red line shows the total radiation field, including both the diffuse and attenuated incident, at the midplane of Component 1. This is the net transmitted continuum, which is the fifth column of the save continuum command in *cloudy*. Similar to Figure 6, the effects of diffuse field within the obscurer are included when making a table of the SED passing through the obscurer. We then used this table to generate the appropriate SED in midplane of Component 1. The EUV and XUV portions of the SED are heavily extinguished so that most radiation at the midplane is due to diffuse gas emission (Figure 9 showed only the diffuse emission).

As is obvious from Figure 1, Component 1 is between the Earth and the obscurer so the obscured Mehdipour et al. (2015) SED is what strikes Component 1. The original continuum used here (Figures 3 and 4 red curve) is now available in

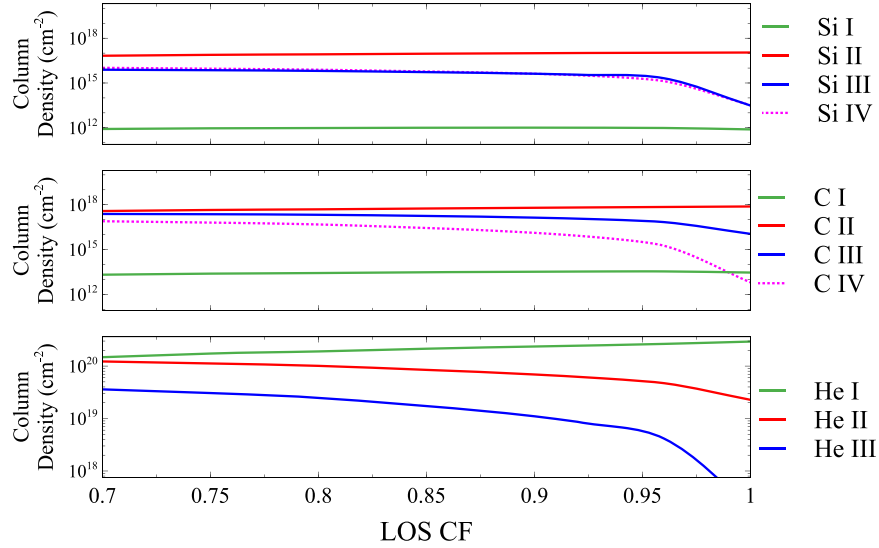


**Figure 8.** Variations of the column densities of different ionization stages as the obscurer LOS CF changes. Si, C, and He are shown in three panels, from top to bottom, respectively.

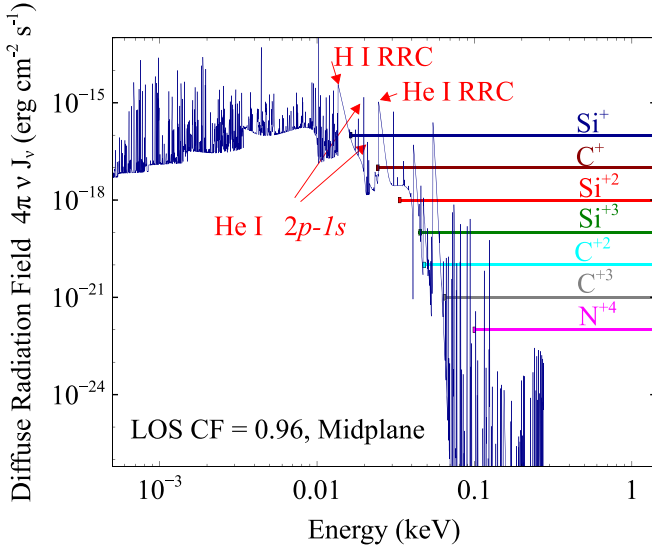


**Figure 9.** Diffuse emission field at the midplane of Component 1 with 96% obscuration. The left terminus of the horizontal lines shows the minimum energy needed to destroy the ion and produce the higher stage ion. RRC stands for radiative recombination continua and H I RRC is the Lyman continuum emission.

Cloudy version 17. This observed continuum is quite a bit harder than the SED in Figure 1 of Mathews & Ferland (1987). The latter was based on observations of very luminous Palomar/Green quasars. The SED adopted here is based on observations of NGC 5548 obtained in 2013 and 2014 by the Anatomy and STORM campaigns. It is worth mentioning that tests show that the choice of intrinsic SED has very little effect on our predictions, which mainly depend on the properties of the obscurer.

To summarize, we have investigated, in detail, how changes in the LOS CF affect the ionization of the higher-ionization species observed by *HST* and identified a unique physical cycle. The LOS CF changes the soft X-ray part of the SED but not the FUV continuum, so the resulting changes would not correlate with the FUV. The soft X-rays change the ionization of helium. The ionizing radiation emitted by recombining  $\text{He}^+$

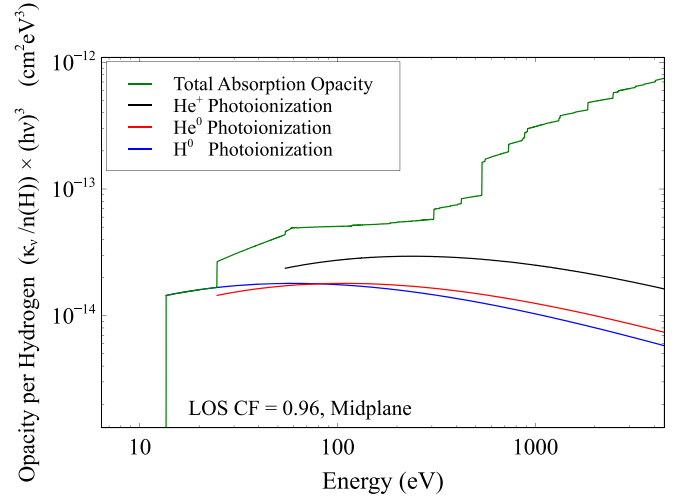


**Figure 10.** Opacity per hydrogen atom is shown as a function of energy. This shows the total opacity at the Component 1 midplane. The vertical axis has been scaled by  $h\nu^3$  for clarity, as described in the text.

changes the ionization rate and abundance of the decorrelated species. However, anything that changes the soft X-rays without affecting the FUV could have a similar effect. This might include the Comptonization scenario outlined by Mathur et al. (2017), the Falling Corona Model studied by Sun et al. (2018) the partial dust obscuration model of Gaskell & Harrington (2018), or other models such as nonaxisymmetric continuum (Dexter & Agol 2011) or anisotropic continuum models (Gaskell & Klimek 2003).

## 7. Testing the Covering Factor Model

In this paper, we did not try to model any particular observation but examined how changes in the obscurer can affect parts of the SED and result in the observed correlated/decorrelated behavior. We have identified a physical cycle that can reproduce the observed behavior. Here we outline two observational tests of this model.

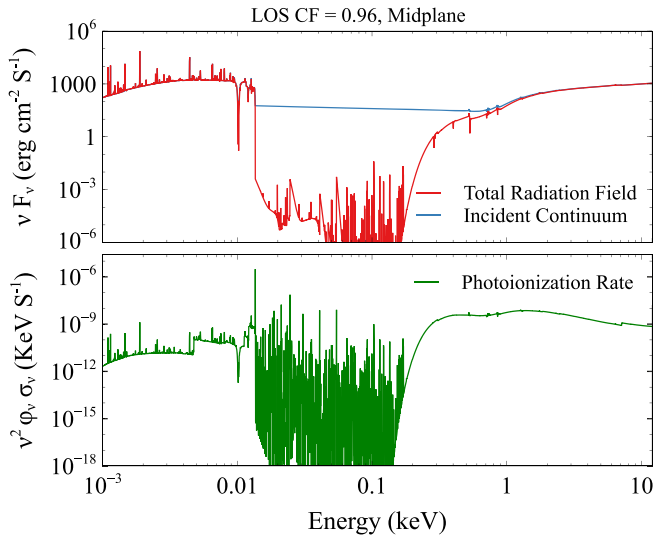


**Figure 11.** Upper panel shows the radiation field striking Component 1 as the blue line and the radiation field at the midplane of the cloud as the red line. The lower panel shows the photoionization rate at each energy.

### 7.1. Existing Observations: The X-Ray Hardness Ratio and Inferred LOS CF

Figure 12 summarizes *Swift* and *HST* observations described by G. A. Kriss et al. (2019, in preparation). The red line is the *HST* continuum at 1367 Å, the blue line shows Ly $\alpha$  absorption line and N V absorption line in the upper and lower panels, respectively. These are examples of correlated and decorrelated lines. These are similar to the blue line in the panels of Figure 2. In our model, the changing obscurer covering factor is responsible for the absorption line holiday. The X-ray hardness ratio measured by *Swift*, a measure of the hard to soft X-ray brightness, is also a measure of the LOS covering factor, as demonstrated by Mehdipour et al. (2016), Equation (2). The obscurer LOS CF changes, derived by Mehdipour et al. (2016) using the broadband spectral modeling of the *Swift* data, are shown in Figure 12 as a green line for comparison. The right CF axis is inverted, decreasing from bottom to top, to make it easier to compare with the other quantities plotted. The upper panel shows that the Ly $\alpha$  absorption line is correlated with the *HST* continuum. The LOS CF is also shown in that panel but with a thinner line to not divert attention. The lower panel is drawn similarly, showing that N V absorption line has a better anticorrelation with the LOS CF rather than the correlation with the *HST* continuum.

Figure 12 shows that N V absorption responds to variations of the LOS CF better than the *HST* continuum. Figure 7 shows that larger covering factors and greater extinction cause N V absorption to weaken: the N V absorption line is predicted to be anticorrelated with the covering factor. These trends are in the same sense as our predictions.

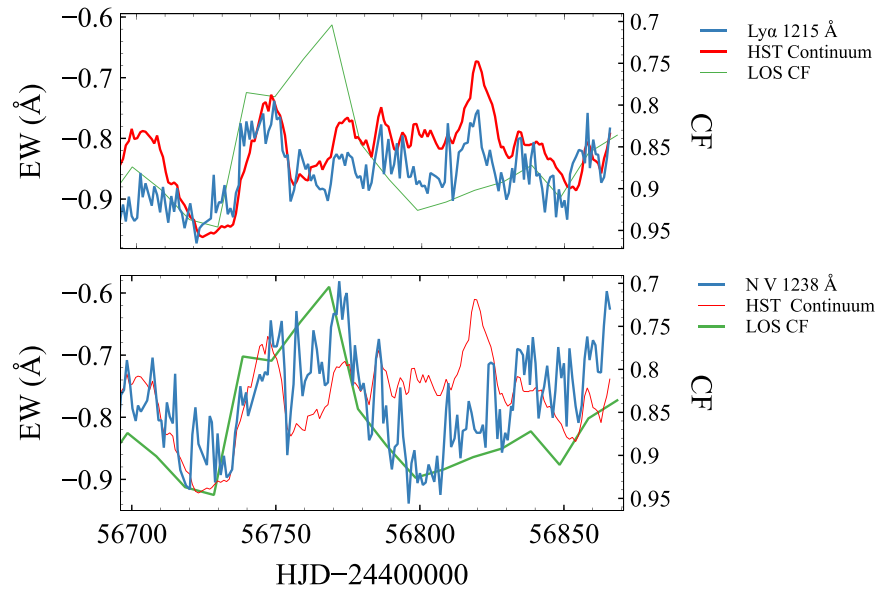
### 7.2. Future Observations: The Full Range of Obscurer Covering Factor

Figure 7 focuses on large values of the LOS CF because the covering factor was in this range during the holiday (Mehdipour et al. 2016). There were other times when the obscurer was not present. Although this was not observed, there must have been times when the obscurer was first coming into our line of sight, and the LOS CF was increasing from

small values. Figure 13 illustrates the full range of the covering factor. The behaviors of the correlated and decorrelated species are reversed for values of LOS CF in the range 0.3–0.5: the correlated species show dramatic changes while the decorrelated ones remain almost constant. Very small values of the LOS CF represented times before 2011 when there was no obscurer. As Figure 13 shows, lower-ionization-potential species almost disappear. Observations that were performed before 2011 confirm the predictions of Figure 13 (Crenshaw et al. 2009). This motivates future observational tests. Continued monitoring of NGC 5548 by *Swift* could identify times when the LOS CF becomes small again. *HST* observations could then be obtained to follow changes in the absorption lines.

## 8. Summary

The reverberation mapping method relies on a causal connection between variations in the lines and continuum. This correlation broke down during the so-called “holiday” period as discovered by the AGN STORM project. The complications due to these abnormalities may have an effect on derived BLR radii and BH masses, which is why it is important to identify the physics that allows such holidays to occur. The fact that high-ionization absorption lines displayed the holiday while low-ionization absorption lines did not is an important clue to what is happening. It is worth emphasizing that “holiday” was first seen in the broad emission-lines, which have a more complicated geometry (Goad et al. 2016). We showed that changes in the luminosity of the AGN do not produce the observed behavior. This suggests that changes in the shape of the SED are responsible. Strong soft X-ray absorption, produced by a transient cloud referred to as the obscurer, was present throughout the AGN STORM campaign. The obscurer covered only a fraction of the continuum source, which we refer to as the “line-of-sight covering factor,” LOS CF. The soft X-ray absorption was not present before 2011, showing that the LOS CF can change dramatically. We investigated the effect of a changing SED on Component 1 cloud producing the strong absorption lines. We have shown that changes in the LOS CF reproduce the observed behavior for large values of the LOS CF. We identified a unique physical cycle in which changes in the LOS CF have a significant effect on the soft X-ray portion of the SED. This changes the ionization stage of helium and the ionizing radiation produced as helium recombines drives the changes in the decorrelated absorption lines. Changes in the LOS CF do not affect the optical or UV continuum because the obscurer is transparent at these energies. We identified two tests of this model. The first is the *Swift* measurements of the X-ray hardness ratio. This can be converted into an obscurer covering factor. This LOS covering factor does seem to correlate with the high-ionization “decorrelated” absorption lines. We show that the sense of the correlation/decorrelation reverses for smaller covering fractions in the range 0.3–0.5, which can be used to test this scenario in future observations. The tests would have to take place when the covering factor is very low. The photoionization models we produced used a variable covering factor to change the soft X-ray portion of the SED. However, other models in which the soft X-ray part of the SED changes independently of the optical/UV continuum could produce similar effects. The Comptonization model proposed by Mathur et al. (2017) and the Falling Corona Model of



**Figure 12.** EW of the Ly $\alpha$  absorption line in Component 1 is shown as the blue line in the upper panel and the EW of the corresponding N V absorption line is shown in the lower panel. The red line shows the *HST* FUV continuum while the green line is the LOS covering factor of the obscurer derived from the X-ray hardness ratio as defined by Mehdipour et al. (2016). The Ly $\alpha$  absorption line is correlated with the *HST* continuum, while N V absorption line anticorrelates with the covering factor.

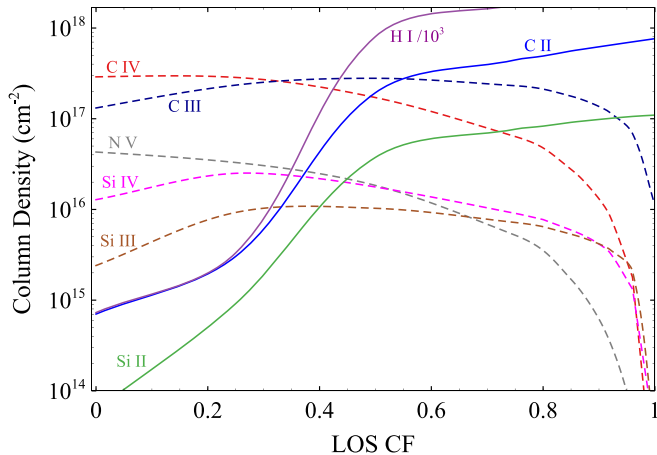


**Figure 13.** Effects of changes in the LOS CF on the ionic column densities over the full range of covering factor are shown. The dashed and solid lines indicate decorrelated and correlated species, respectively. Their behavior swaps around in the low and high covering factor limits, offering a test of the variable covering factor model. In this model, the ionization parameter for Component 1 is  $\log U = -1.5$ .


Sun et al. (2018) could also produce the required changes in the SED. This will be the subject of future work.

Support for *HST* program number GO-13330 was provided by NASA through a grant from the Space Telescope Science Institute, which is operated by the Association of Universities for Research in Astronomy, Inc., under NASA contract NAS5-26555. We thank NSF (1816537), NASA (ATP 17-0141), and STScI (*HST*-AR.13914, *HST*-AR-15018) for their support and Huffaker scholarship for funding the trip to Atlanta to attend the annual AGN STORM meeting, 2017. M.C. acknowledges support from NASA through STScI grant *HST*-AR-14556.001-A and STScI grant *HST*-AR-14286. M.D., G.F., and F.G. acknowledge support from the NSF (AST-1816537), NASA (ATP 17-0141), and STScI (*HST*-AR-13914, *HST*-AR-15018), and the Huffaker Scholarship. B.M.P., G.D.R., M.M.F, C.J.G.,

and R.W.P. are grateful for the support of the National Science Foundation through grant AST-1008882 to The Ohio State University. A.J.B. has been supported by NSF grant AST-1412693. M.C.B. gratefully acknowledges support through NSF CAREER grant AST-1253702 to Georgia State University. S.B. is supported by NASA through the *Chandra* award no. AR7-18013X issued by the *Chandra* X-ray Observatory Center, operated by the Smithsonian Astrophysical Observatory for and on behalf of NASA under contract NAS8-03060. S.B. was also partially supported by grant *HST*-AR-13240.009. E.D.B. acknowledge support from Padua University through grants DOR1699945/16, DOR1715817/17, DOR1885254/18, and BIRD164402/16. K.D.D. is supported by an NSF Fellowship awarded under grant AST-1302093. R.E. gratefully acknowledges support from NASA under the ADAP award 80NSSC17K0126. K.H. acknowledges support from STFC grant ST/R000824/1. SRON is financially supported by NWO, the Netherlands Organization for Scientific Research. C.S.K. acknowledges the support of NSF grant AST-1009756. A.P. is supported by NASA through Einstein Postdoctoral Fellowship grant number PF5-160141 awarded by the *Chandra* X-ray Center, which is operated by the Smithsonian Astrophysical Observatory for NASA under contract NAS8-03060. T.T. has been supported by NSF grant AST-1412315. T.T. and B.C.K. acknowledge support from the Packard Foundation in the form of a Packard Research Fellowship to T.T. The American Academy in Rome and the Observatory of Monteporzio Catone are thanked by T.T. for kind hospitality. M.V. gratefully acknowledges support from the Danish Council for Independent Research via grant No. DFF 4002-00275. This research has made use of the NASA/IPAC Extragalactic Database (NED), which is operated by the Jet Propulsion Laboratory, California Institute of Technology, under contract with the National Aeronautics and Space Administration. I.McH. acknowledges support from a Royal Society Leverhulme Trust Senior Research Fellowship LT160006 and from STFC grant ST/M001326/1. J.M.G. gratefully acknowledges support from NASA under awards

NNX15AH49G and 80NSSC17K0126. E.D.B. acknowledges support from Padua University through grants DOR1699945/16, DOR1715817/17, and DOR1885254/18.

### ORCID iDs

M. Dehghanian  <https://orcid.org/0000-0002-0964-7500>  
 G. J. Ferland  <https://orcid.org/0000-0003-4503-6333>  
 G. A. Kriss  <https://orcid.org/0000-0002-2180-8266>  
 B. M. Peterson  <https://orcid.org/0000-0001-6481-5397>  
 F. Guzmán  <https://orcid.org/0000-0002-2915-3612>  
 P. A. M. van Hoof  <https://orcid.org/0000-0001-7490-0739>  
 R. J. R. Williams  <https://orcid.org/0000-0002-0486-0580>  
 A. J. Barth  <https://orcid.org/0000-0002-3026-0562>  
 M. C. Bentz  <https://orcid.org/0000-0002-2816-5398>  
 S. Bisogni  <https://orcid.org/0000-0003-3746-4565>  
 W. N. Brandt  <https://orcid.org/0000-0002-0167-2453>  
 D. M. Crenshaw  <https://orcid.org/0000-0002-6465-3639>  
 G. De Rosa  <https://orcid.org/0000-0003-3242-7052>  
 M. M. Fausnaugh  <https://orcid.org/0000-0002-9113-7162>  
 A. Gupta  <https://orcid.org/0000-0003-1880-1474>  
 Keith Horne  <https://orcid.org/0000-0003-1728-0304>  
 J. Kaastra  <https://orcid.org/0000-0001-5540-2822>  
 K. T. Korista  <https://orcid.org/0000-0003-0944-1008>  
 R. W. Pogge  <https://orcid.org/0000-0003-1435-3053>  
 M. Vestergaard  <https://orcid.org/0000-0001-9191-9837>

### References

- Arav, N., Chamberlain, C., Kriss, G. A., et al. 2015, *A&A*, **577**, 37  
 Cappi, M., De Marco, B., Ponti, G., et al. 2016, *A&A*, **592**, A27  
 Crenshaw, D. M., Kraemer, S. B., Gabel, J. R., et al. 2003, *ApJ*, **594**, 116  
 Crenshaw, D. M., Kraemer, S. B., Schmitt, H. R., et al. 2009, *ApJ*, **698**, 281  
 Cruddace, R., Paresce, F., Bowyer, S., & Lampton, M. 1974, *ApJ*, **187**, 497  
 De Rosa, G., Peterson, B. M., Ely, J., et al. 2015, *ApJ*, **806**, 128  
 Dexter, J., & Agol, E. 2011, *ApJ*, **727L**, 24D  
 Di Gesu, L., Costantini, E., Ebrero, J., et al. 2015, *A&A*, **579**, A42  
 Ebrero, J., Kaastra, J. S., Kriss, G. A., et al. 2016, *A&A*, **587**, A129  
 Edelson, R., Gelbord, J. M., Cackett, E., et al. 2019, *ApJ*, **870**, 123  
 Edelson, R., Gelbord, J. M., Horne, K., et al. 2015, *ApJ*, **806**, 129  
 Fausnaugh, M. M., Denney, K. D., Barth, A. J., et al. 2016, *ApJ*, **821**, 56  
 Ferland, G. J., Chatzikos, M., Guzmán, F., et al. 2017, *RMxAA*, **53**, 385  
 Ferland, G. J., & Mushotzky, R. F. 1982, *ApJ*, **262**, 564  
 Gardner, E., & Done, C. 2017, *MNRAS*, **470**, 3591  
 Gaskell, C. M. 2017, *MNRAS*, **467**, 226  
 Gaskell, C. M., & Harrington, P. Z. 2018, *MNRAS*, **478**, 1660  
 Gaskell, C. M., & Klimek, E. S. 2003, *A&AT*, **22**, 661G  
 Goad, M., Korista, K. T., De Rosa, G., et al. 2016, *ApJ*, **824**, 11  
 Hopkins, P. F., Strauss, M. A., Hall, P. B., et al. 2004, *AJ*, **128**, 1112  
 Kaastra, J. S., Kriss, G. A., Cappi, M., et al. 2014, *Sci*, **345**, 64  
 Kaastra, J. S., Mewe, R., Liedahl, D. A., et al. 2000, *A&A*, **345**, L83  
 Kallman, T., & Bautista 2001, *ApJS*, **133**, 221  
 Leighly, K. M. 2004, *ApJ*, **611**, 125  
 Lodders, K. 2003, *ApJ*, **591**, 1220  
 Mathews, W. G., & Ferland, G. J. 1987, *ApJ*, **323**, 456M  
 Mathur, S., Elvis, M., & Wilkes, B. 1995, *ApJ*, **452**, 230  
 Mathur, S., Elvis, M., & Wilkes, B. 1999, *ApJ*, **519**, 605  
 Mathur, S., Gupta, A., Page, K., et al. 2017, *ApJ*, **846**, 55  
 Mehdipour, M., Kaastra, J. S., Kriss, G. A., et al. 2015, *A&A*, **575**, 22  
 Mehdipour, M., Kaastra, J. S., Kriss, G. A., et al. 2016, *A&A*, **588**, 139  
 Osterbrock, D. E., & Ferland, G. J. 2006, *Astrophysics of Gaseous Nebulae and Active Galactic Nuclei* (2nd ed.; Sausalito, CA: Univ. Science Books)  
 Pei, L., Fausnaugh, M. M., Barth, A. J., et al. 2017, *ApJ*, **837**, 131  
 Peterson, B. M., Denney, K. D., De Rosa, G., et al. 1999, *ApJL*, **521**, L95  
 Ride, S. K., & Walker, J. R. 1977, *A&A*, **61**, 347  
 Starkey, D., Horne, K., Fausnaugh, M. M., et al. 2017, *ApJ*, **835**, 65  
 Sun, M., Xue, Y., Cai, Z., & Guo, H. 2018, *ApJ*, **857**, 86  
 Tarter, C. B., Tucker, W. H., & Salpeter, E. E. 1969, *ApJ*, **156**, 943  
 Ursini, F., Boissay, R., Petrucci, P.-O., et al. 2015, *A&A*, **577**, A38  
 Whewell, M., Branduardi-Raymont, G., Kaastra, J. S., et al. 2015, *A&A*, **581**, A79